Journal of Electronic Materials (2022) 51:5842–5856
https://doi.org/10.1007/s11664-022-09804-3

ORIGINAL RESEARCH ARTICLE

Effect of PVP Assisted Growth of α-Mn_2O_3 Nanoparticles on the Structural, Microstructural, Magnetic and Optical Properties

Kavita Kumari[1] · Shalendra Kumar[2,3] · Seok-Hwan Huh[4] · Akshay Kumar[5] · Min-Soo Kim[6] · Min-Ji Shin[5] · Nirmla Devi[7] · Bon-Heun Koo[1,5]

Received: 20 October 2021 / Accepted: 28 June 2022 / Published online: 8 August 2022

Abstract

Single-phase manganese oxide, α-Mn_2O_3 , nanoparticles have been prepared successfully using different amounts of 2w/v% polyvinylpyrrolidone (PVP) via co-precipitation. The samples prepared with 1 ml, 2 ml, 5 ml and 10 ml PVP are represented as S1, S2, S3 and S4, respectively. The effect of PVP amount on the structural, microstructural, magnetic and optical properties was systematically investigated. Rietveld refinement of the x-ray diffraction patterns revealed the single-phase formation of α-Mn_2O_3 nanoparticles. The average crystallite sizes of the particles was found to be minimum for S2 with lowest lattice parameter and highest strain. High-resolution field emission scanning electron microscopy confirmed the smallest size of S2 with spherical morphology and smooth surfaces. Energy dispersive x-ray spectroscopy and maps showed uniform distribution of the elements favouring the Mn_2O_3 composition. Raman and Fourier transform infrared spectra displayed characteristic bands corresponding to α-Mn_2O_3. The magnetic susceptibility revealed the antiferromagnetic nature of α-Mn_2O_3 nanoparticles with Néel temperature, T_N ~ 80.6 K for S2. The increase in PVP amount above 2 ml increased the T_N as well as the magnetic frustration. The band gap was found to be maximum (1.8 eV) for S2 nanoparticles. Briefly, the smallest size nanoparticles with spherical shape and smooth surfaces were obtained for 2 ml PVP with the lowest magnetic frustration and highest band gap indicating the optimum amount of PVP to be 2 ml. Thereby, the results have revealed the limiting behaviour of polyvinylpyrrolidone chains operating during synthesis.

Keywords Polyvinylpyrrolidone (PVP) · cubic α-Mn_2O_3 nanoparticles · rietveld refinement · band gap · antiferromagnetic

✉ Bon-Heun Koo
bhkoo@changwon.ac.kr

1 Industrial Technology Research Institute, Changwon National University, Changwon, Gyeongnam 51140, Republic of Korea

2 Department of Physics, College of Science, King Faisal University, P.O Box400, Hofuf, Al-Ahsa 31982, Saudi Arabia

3 Department of Physics, University of Petroleum and Energy Studies, Dehradun 248007, India

4 Department of Mechatronics Conversion Engineering, Changwon National University, Changwon, Gyeongnam 51140, Republic of Korea

5 Department of Materials Convergence and System Engineering, Changwon National University, Changwon, Gyeongnam 51140, Republic of Korea

6 School of Advanced Defense Engineering College of Interdisciplinary Cooperative Process, Changwon National University, Changwon, Gyeongnam 641-773, Republic of Korea

7 Suraj PG Degree College, Sec – 75, Gurugram, Haryana 122103, India

Introduction

Manganese oxides have gained a great deal of attention from the scientific community due to their promising industrial applications in the domains of nanotechnology,[1] electrochemistry[2,3] and biochemistry.[4] The manganese oxides can form stable structures with various oxidation states, Mn^{2+}(MnO), Mn^{3+}(Mn_2O_3), Mn^{2+}/Mn^{3+}(Mn_3O_4), Mn^{4+}(MnO_2) and with various crystallographic symmetries such as cubic (space group: *Ia3*) , tetragonal (*I4/m*), and orthorhombic (space group: *Pbca*)[5–10] at room temperature, which makes it an interesting material displaying immense possibilities for modifications in structural, electronic structural, optical, magnetic, electrochemical and physicochemical properties.[5,11–14] Among all the manganese oxides, Mn_2O_3, also known as bixbyite, is one of the most stable antiferromagnetic (AFM) states with more than one transition in the range 20-80 K: one ferromagnetic state at ~ 43 K and another antiferromagnetic state at ~ 80 K.[6]

Mn_2O_3 exists with two polymorphs, α-Mn_2O_3 and β-Mn_2O_3 out of which α-Mn_2O_3 possesses a peculiar electronic structure with MnO_6 octahedral sites on the surface showing a high possibility of structural distortions.[3] The presence of anti-bonding e_g^1 configuration of Mn^{3+} in MnO_6 octahedra are likely to cause variation in the Mn-O and Mn-Mn bond lengths developing structural versatility in Mn_2O_3. In addition, the structure of α-Mn_2O_3 exhibits two phases: orthorhombic below 302 K and cubic above 302 K.[15–17] Moreover, the antiferromagnetic nature of Mn_2O_3 arises due to the interaction between the adjacent MnO_6 octahedra.[18,19] As a consequence of interesting structural adaptabilities and antiferromagnetic nature, Mn_2O_3 -based composites such as Mn_2O_3/NiO,[20] Mn_2O_3-Co_2O_3,[21] Mn_2O_3-SnO_2,[22] Mn_3O_4/Mn_2O_3 nanoclusters[23,24] exhibit immense potential for various technological applications.[6]

Furthermore, the efficiency of Mn_2O_3 -based devices can be upgraded by improving the properties of Mn_2O_3 nanostructures. For instance, the manganese oxides are used as electrode materials for the supercapacitor applications, and by improving the efficiency of these electrodes, the performance of supercapacitors can be enhanced.[6] Synthesis through chemical methods is favorable due to the extensive scope to improve the properties of nanostructures during the chemical reactions through structural, electronic structural and morphological modulations. In order to achieve enhanced properties, the utilization of various types of surfactants and stabilizers have proved to be advantageous due to their tendency to stabilize as well as control the particle size and morphology.[25,26] The usage of surfactants during synthesis not only prevents agglomeration but can also improve the properties of the material. For instance, PVP has been found to effectively prevent the agglomeration of Ag nanoparticles in addition to hampering their growth.[25,27,28]The size of nickel nanoparticles was controlled using PVP as reported by Tientong et al.[29]Likewise, Amsaveni et al. prepared Mn_2O_3 nanoparticles using CTAB (cetyltrimethylammonium bromide) and obtained good optical and catalytic properties.[4] Thus, these reports suggest that the increasing amount of surfactant proportionally reduces the size of the particles and accordingly influences the related properties. However, very few reports put forward that there is a limit to the amount of the surfactant or stabilizer that can give desired properties of the material. For instance, Khor et al. reported that the extempore use of HMTA (hexamethylenetetramine) can result in sedimentation of the metals.[30] Likewise, Li et al. found that the size of barium titanate nanoparticles first decreased with increasing concentration of PVP from 0 to 300 g/L, but then increased on increasing the PVP concentration beyond 300 g/L.[31]

Therefore, in order to understand the limiting behaviour of the amount of surfactant used to control the growth of nanoparticles, we have synthesized Mn_2O_3 nanoparticles using different amounts of 2w/v% PVP solution in the present work and investigated their structural, microstructural, optical and magnetic properties. Simple co-precipitation method was followed for the synthesis of the nanoparticles which does not require the use of hazardous chemicals, high temperatures or pressures. The synthesized nanoparticles were characterized through XRD, HR-FESEM, Raman spectroscopy, FTIR spectroscopy, magnetization and UV-vis absorption spectroscopy in order to investigate the effect of different PVP amounts on various properties of the nanoparticles.

Experimental Methods

Chemicals Required

Mn_2O_3 nanoparticles were synthesized using Mn $(NO_3)_2xH_2O$ (178.95 g/mol), ammonia solution (35.04 g/mol), and polyvinylpyrrolidone (PVP)—K30 (40000 g/mol). All the chemicals were purchased from Sigma Aldrich with purity > 97%.

Synthesis Procedure

The Mn_2O_3 nanoparticles were prepared using co-precipitation method. Two solutions were prepared simultaneously: solution 1 and solution 2. To prepare solution 1, 0.1 M of hydrated manganese nitrate was dissolved in 100 ml of DI water. The mixture was stirred magnetically at room temperature for homogeneous mixing. After 1 h of mixing, the ammonia solution was added dropwise up to a pH of 9. To prepare solution 2, 2 g of PVP K30 was dissolved in DI water for a final volume of 100 ml in order to make 2w/v% PVP solution. After 30 min, 1 ml of solution 2 was added dropwise into solution 1. The stirring continued at room temperature for 24 h. Afterwards, the precipitates were separated through centrifugation followed by washing several times with DI water and ethanol. After washing, the precipitates were dried at 50°C in a hot-air oven for 18 h. Thus-obtained precipitates were ground and annealed at 500°C for 2 h in an open-box furnace. Similarly, the samples were prepared with 2 ml, 5 ml and 10 ml PVP. Thus-synthesized samples are labelled as sample with 1 ml PVP, S1; sample with 2 ml PVP, S2; sample with 5 ml PVP, S3; sample with 10 ml PVP, S4.

Characterization

The resultant products were characterized using various techniques viz. x-ray diffraction (XRD), high-resolution field emission scanning electron microscopy (HR-FESEM), energy dispersive x-ray spectroscopy (EDS), Raman

spectroscopy, Fourier transform infrared (FTIR) spectroscopy, dc-magnetization and UV-Vis absorption spectroscopy. The XRD patterns were obtained using a PANalytical X'pert Pro x-ray diffractometer ($\lambda_{Cu\text{-}K\alpha} = 0.15406$ nm) in the range $20° \leq 2\theta \leq 80°$ (step size = 0.016715° and scan speed = 1 s). HR-FESEM micrographs and EDS maps were scanned using a Merlin compact at 5 kV and 15 kV, respectively. To acquire the EDS maps, the surfaces of the samples were coated with platinum which acted as the conducting agent. The coating was performed for a time period of 180 s. The Raman spectra were obtained using a JASCO NRS-3300 laser Raman spectrometer at room temperature. The laser source with wavelength ~ 532.24 nm (laser power: 3.9 mW, exposure time: 10 s) was employed to collect the samples. FTIR spectra were measured using a FTIR-4200 from 15,000 to 20 cm^{-1} at room temperature. The magnetization measurements were carried out using the VSM module of the cryogen-free VersaLab developed by Quantum Design. The UV-Vis absorption spectra were obtained using a V-670 spectrophotometer.

Results and Discussion

Structural Analysis

The phase formation and crystallographic information of the synthesised nanoparticles are obtained from the investigation of XRD patterns through Rietveld refinement performed using the FullProf Suite program.[32] Figure 1 displays the Rietveld refinement of the sharp and precisely defined diffraction peaks indicating the nanocrystalline nature of the samples. The black data points represent the observed patterns while the superimposed red lines represent the theoretically calculated patterns. The vertical green lines designate the Bragg positions of the reflecting planes. The difference between the observed and calculated patterns is indicated at the bottom of all the patterns with the blue line. The enlarged view of the fitted experimental and theoretical data points is displayed in the inset of Fig. 1. The Rietveld refinement is helpful to get important information about the crystal structure through indexing of the pattern, determination of the crystal symmetry, space group, intensities, lattice parameters and full width at half maxima (FWHM).[33] Indexing of the peaks has been done using the refined Bragg positions. The nanoparticles are found to possess cubic symmetry with space group Ia3 corresponding to the α-Mn_2O_3 phase of the bixbyite in accordance with the JCPDS number 65–7467 displayed in the lowest stack of Fig. 1.[34,35] The planes assigned to the peaks are marked in the diffractogram (see Fig. 1). No foreign peak was detected corresponding to PVP, secondary phases of manganese oxide or any other impurities indicating the single-phase nature of the nanoparticles.

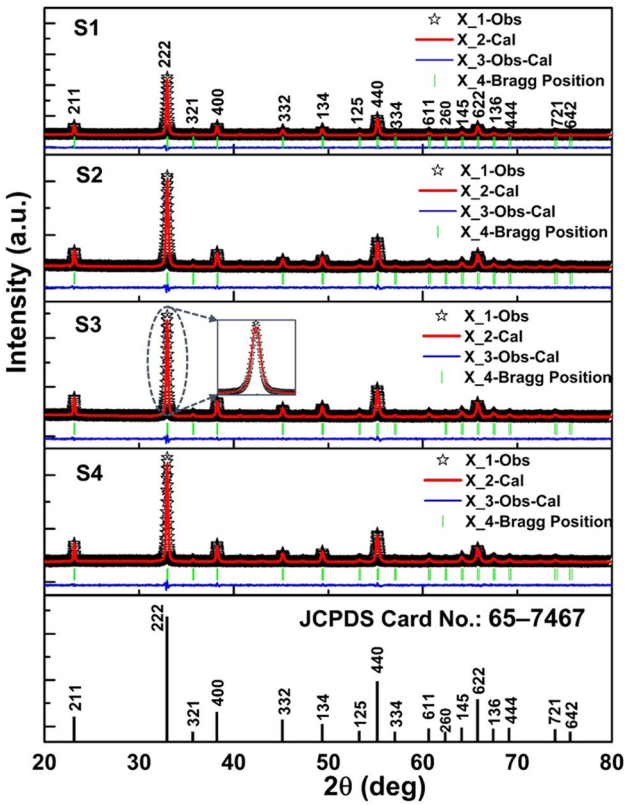

Fig. 1 Rietveld refined patterns of samples S1 to S4 and JCPDS card number 65-7467 of α-Mn_2O_3 (lowest stack); the black line indicates the experimentally observed data points, the red line refers to the theoretically calculated patterns, the blue line indicates the difference between the two, the vertical green lines are the Bragg positions; inset shows the enlarged portion of peak (222) demonstrating the fitting of observed and calculated data points (Color figure online).

To obtain the values of the structural parameters, it is very important to assess the quality of fitting of the refined patterns, both qualitatively and quantitatively. The qualitative information about the quality of fitting can be observed by checking the difference between the observed and calculated patterns. The smaller the difference, the better the fitting. This difference is very small for all the samples in the present case as shown by the blue lines (see Fig. 1). Further, the quantitative information about the quality of fitting can be obtained using some statistical parameters such as agreement factors, also known as reliability factors (*R-factors*) and χ^2 values. To determine the values of these statistical parameters, the refinement procedure follows the least-squares approach to minimise the errors between the observed and the theoretically calculated data in order to achieve least-squares fit. This is done by minimizing a residual function which estimates the values of the *R-factors.*

This provides a good criterion to determine the quality of the refinement. The *R-factors* are estimated as R_p, R_{wp} *and* R_e which represent the profile, weighted and expected values of the *R-factors*.[33,36]

The values of *R-factors* quantify the quality of the refinement and are displayed in Table I. Out of all these parameters, R_{wp} is of most importance because it comes directly from the square root of the weighted minimized quantity. For an ideal case, the value of R_{wp} is expected to be 1. But practically it is difficult to achieve; therefore, we look for the best possible value, i.e., R_{exp} that can be achieved. In the present case, the obtained value of R_{wp} ~ 1.6 and R_p ~ 1.1, which are acceptable and indicate good quality fitting. The ratio of R_{wp}/R_{exp} reveals the "goodness of fit" and is indicated by the parameter χ^2. The refinement should converge at $\chi^2 > 1$ and it should never be less than 1. $\chi^2 = 1$ is the ideal case. χ^2 less than 1 indicates that the parameters may have been over-refined or too many unnecessary parameters have been introduced. Similarly, very large values of χ^2 (>> 1) indicate the under-refined parameters. A value of χ^2 is slightly greater than 1 (χ^2>1) is acceptable; however, this still does not assure the correctness of the model because the correctness of the model also depends on other factors of refinement such as *R-factors*. The accuracy of these statistical parameters is governed by observing them throughout the refinement process.[37] The guidelines followed during the refinement procedure are well described by McCusker et al.[38] The fitting in the present case converged with χ^2 ~ 1.1 for all samples (Table I). Thus, the overall acceptable values of the statistical parameters and the small difference between the observed and calculated patterns shows the good quality of fitting of the XRD patterns. In addition, the refined structure of cubic α-Mn_2O_3 corresponding to sample S2, with $x_{min} = z_{min} = -0.1$; $x_{max} = z_{max} = 1.1$ and $y_{min} = y_{max} = 0.0$, is displayed in Fig. 2a.

Table I *R*-factors and χ^2 values obtained by Rietveld refinement

Samples	R_p	R_{wp}	R_{exp}	χ^2	R_{Bragg}
S1	1.22	1.63	1.55	1.10	1.30
S2	1.22	1.62	1.53	1.11	0.93
S3	1.23	1.62	1.52	1.14	0.95
S4	1.25	1.64	1.56	1.11	1.07

The small change in lattice parameter can be established from the shift in the peak positions as displayed in Fig. 2b for peak (222). The values of the lattice parameters are demonstrated in Fig. 2c showing that they remain almost the same (~ 9.40 Å) with an uncertainty of ±0.0004 Å. The change in lattice parameter with respect to the PVP amount

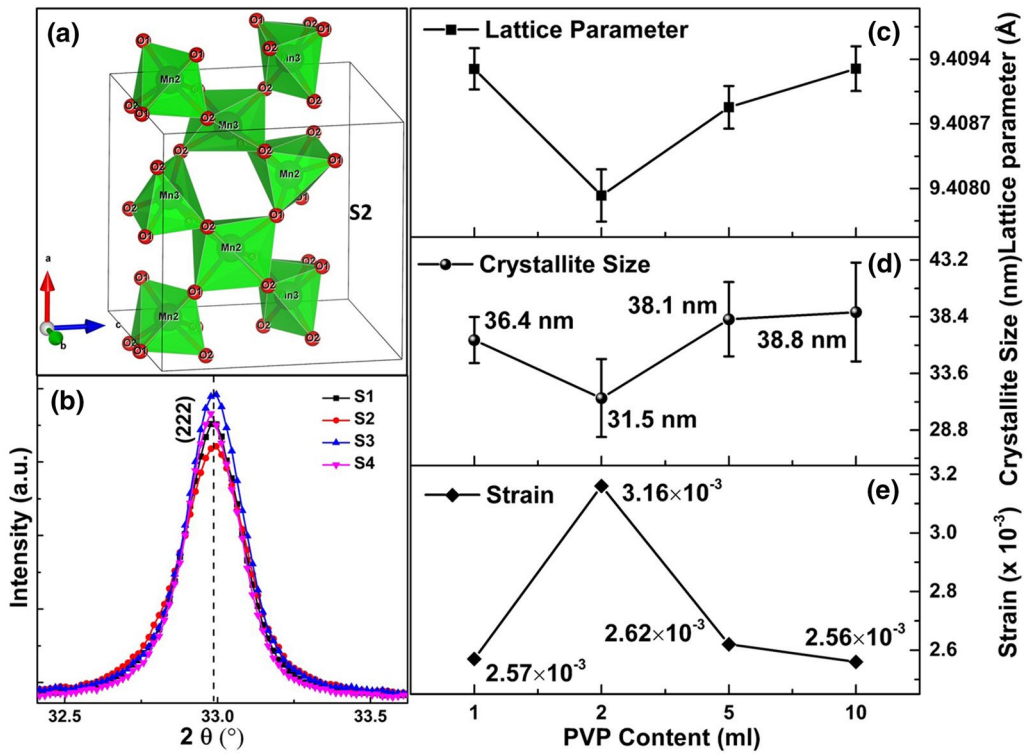

Fig. 2 (a) Crystal structure of sample S2 prepared with 2 ml PVP; (b) Enlarged view of peak (222) of samples S1 to S4 indicating variation in 2θ value as compared to sample S1; (c) Lattice parameters with an uncertainty of ± 0.0004 Å; (d) Crystallite size with an uncertainty of 4.0 nm; (e) Strain displayed relatively for samples S1 (1 ml PVP), S2 (2 ml PVP), S3 (5 ml PVP) and S4 (10 ml PVP).

is small; however, it is supported by the change in peak positions (see Fig. 2b) which are obvious with the increase in cell volume. The lattice parameters obtained in the present case are comparable to the earlier reported values for α-Mn_2O_3. For instance, Son et al.,[35] Karuppaiah et al.[20] and Ribeiro et al.[3] reported the lattice parameter ~ 9.4 Å. Further, the average crystallite sizes (D_{XRD}) and strain (ε) have been calculated using the following equations[39]:

$$D_{\mathrm{XRD}} = \frac{K\lambda}{\beta \mathrm{Cos}\theta} \tag{1}$$

$$\beta = 4\varepsilon \tan\theta \tag{2}$$

where K=0.89 is the shape factor while β and θ are the FWHM and positions of Bragg's reflections, respectively. The values of FWHM and peak positions were obtained from the results of Rietveld refinement. The FWHM depends on the peak shape parameters, U, V and W, which can be described by the expression[38]:

$$\beta^2 = U\tan^2(\theta) + V\tan(\theta) + W \tag{3}$$

The values of the peak shape parameters especially depend on the selection of the peak shape function employed during the refinement procedure which was selected as pseudo-Voigt in the present case. The FWHM corresponding to the significant intensity peaks, (211), (222), (400), (332), (431), (440), and (622), were used to determine the crystallite sizes. The values of the crystallite sizes were found to be 36, 32, 38 and 39 nm for S1, S2, S3 and S4, respectively, as presented in Fig. 2d. The amount of PVP seems to directly influence the crystallite dimensions. The minimum size is obtained to be 32 nm for S2 and a maximum size of 39 nm is obtained for S4. It is evident that the size of the particles decreased when the PVP amount increased from 1 ml to 2 ml, and thereafter it increased progressively with increasing PVP amount. This shows that an adequate amount of PVP is very essential to reduce the crystallite dimensions, beyond which it affects the size in an inverse way indicating the limiting behaviour of PVP chains. The crystallite sizes of the nanoparticles obtained in the present case are comparable to that reported by You-Hyun et al.[35] and Jiao et al.[40] It is interesting to note that Najjar et al. reported the particle sizes of Mn_2O_3 nanoparticles, prepared without adding PVP, ranging from 65 to 111 nm as a function of pH and found the size to be decreasing with increasing pH (9–13), i.e., the smallest size (65.91 nm) was obtained for the highest value of pH (13).[41] However, in our case, the crystallite sizes obtained are below 40 nm for all the samples with a pH value of 9. This confirms the effective assistance of PVP during synthesis. Furthermore, the strain calculated using Eq. 2 is found to vary inversely with the crystallite size. The values of the strain obtained has been demonstrated in Fig. 2e. The inverse relationship between the crystallite size and strain can be observed from Fig. 2d–e which reveals that as the crystallite size decreases, the strain in the lattice increases and vice versa. The strain is found to be maximum (3.16 x 10^{-3}) in the nanoparticles of smallest size and is minimum (2.56 x 10^{-3}) in the nanoparticles with largest size. A possible reason for the development of strain in the nanoparticles is the generation of defects which may be line defects and planar defects/stacking faults. Both types of defects can cause variation in the lattice parameters and strain which is indicated by the change in peak positions of XRD patterns. The line defects can be calculated by the dislocation density using the formula $1/D^2$, where D is the crystallite size.[42] In the present case, the values of the dislocation density have been found to be very low, of the order of 10^{-4} m^{-2} in all the samples, whereas the stacking faults may be estimated using the following equation[43]:

$$\alpha = \frac{\Delta 2\theta}{-45\sqrt{3}/\pi^2}\left[\tan\theta_{222} + \frac{\tan\theta_{321}}{2}\right]^{-1} \tag{4}$$

where $\Delta 2\theta = [\{2\,\theta_{222} - 2\,\theta_{321}\}_{\mathrm{expt}} - \{2\,\theta_{222} - 2\,\theta_{321}\}_{\mathrm{stand}}]$. The values of the stacking faults have been found to be of the order of 10^{-6} for all the samples. The values of both the dislocation density and the stacking faults are too small to be considered significant for introducing the strain. Therefore, it seems that the effect of PVP chain attached to the crystallite is more prominent than the defects in the crystallites. Here, it can be interpreted that the decrease in the crystallite size increases the surface pressure which correspondingly increases the strain. Therefore, the highest strain has been found in the smallest size crystallites. A similar type of relationship between the strain and the nanoparticle size was reported earlier by Deotale et al. who found the maximum strain in the smallest size particles.[44]

Microstructural Analysis

The morphology and particle sizes of the nanoparticles are investigated using the HR-FESEM micrographs as displayed in Fig. 3a–d. The effect of PVP amount on the morphology and size of the nanoparticles can be observed. At a low PVP amount (S1), the morphology deviates from the spherical shape and manifests elongated particles, as can be observed in Fig. 3a. As the PVP amount increases to 2 ml (S2), the morphology becomes more spherical along with the decrease in particle size (see Fig. 3b). However, as the PVP amount is increased beyond 2 ml, the agglomeration of the particles begins and particle size increases (see Fig. 3c–d). Thus, it can be seen from the micrographs that in sample S2, the majority of the particles show a spherical shape and have the smallest size. Further, the average particle sizes have been calculated by fitting the histograms

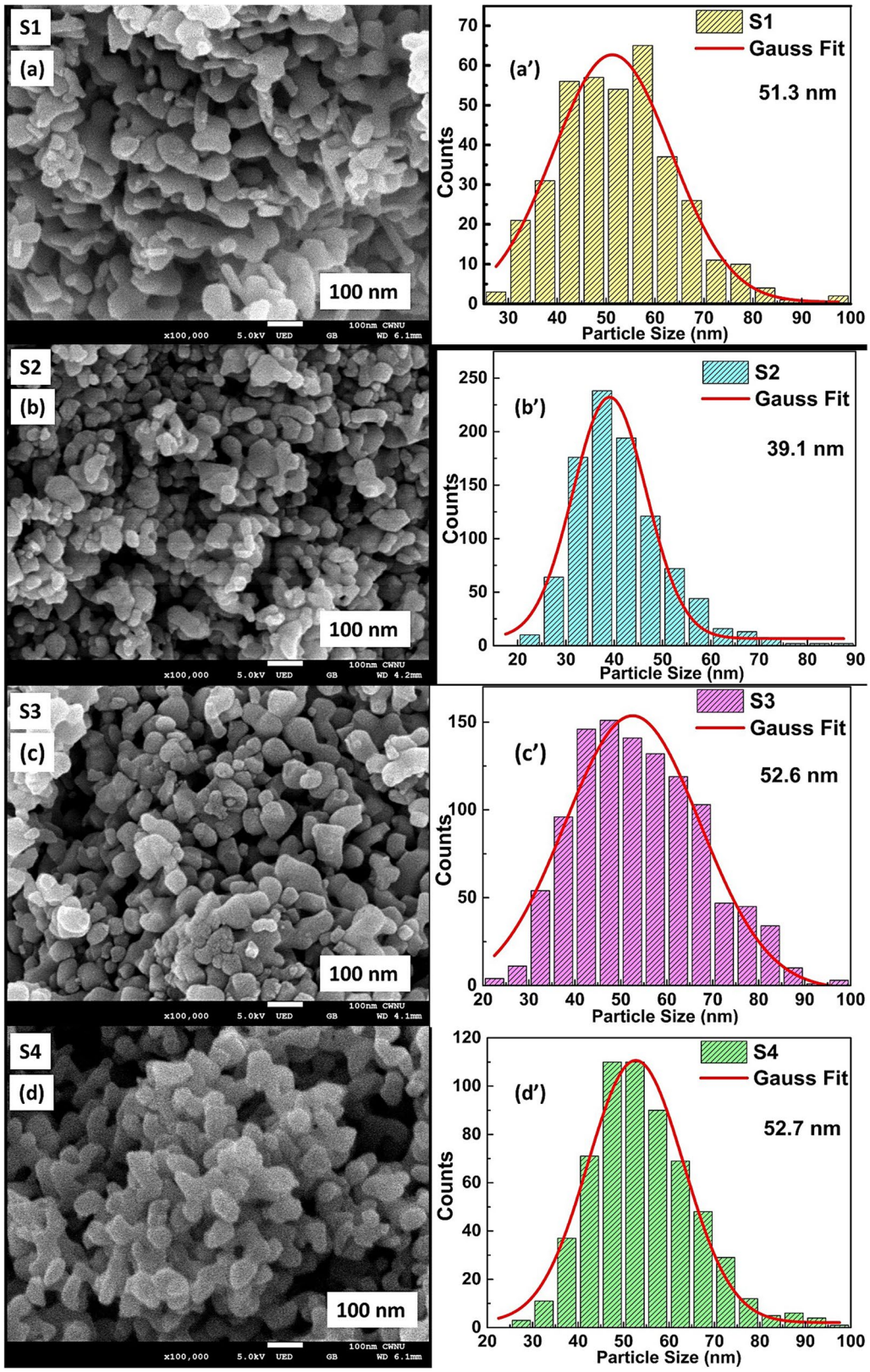

Fig. 3 (a–d) HR-FESEM micrographs of samples S1 to S4, respectively, and (a'–d') fitted histograms displaying particle size distribution; average particle size obtained from fitting are displayed with each histogram.

of particle size distribution which are presented in Fig. 3a'-d'. The histograms show a broad particle size distribution except for sample S2 which demonstrates the narrowest particle size distribution. The narrow size distribution indicates that PVP uniformly influences the growth of a large number of particles. The particle size has been found to decrease when the PVP amount is increased from 1 ml (S1) to 2 ml (S2); however, as the PVP amount is increased beyond 2 ml, the particle size starts increasing and becomes maximum for the sample with 10 ml PVP (S4). The minimum particle size obtained for S2 nanoparticles may be attributed to PVP which acts as a surfactant and hampers the multi-dimensional growth of the nanoparticles.[20] However, when the amount of PVP increases in the aqueous medium, the number of ions within the boundaries of the PVP chains also increases which may lead to the electrostatic repulsions resulting in the increase of the sizes of the nanoparticles.[45] Thus, the minimum particle size is obtained for S2 (39.1 nm) and the maximum particle size is obtained for S4 (52.7 nm). The variation trend of the average particle sizes agrees well with the XRD results.

The elemental composition and atomic % of the nanoparticles have been extracted using energy dispersive x-ray spectroscopic (EDS) analysis. The EDS spectra of all the samples along with the atomic % and element distribution maps are displayed in Fig. 4a–d which provides the qualitative information of the chemical composition of the samples.[46] In the maps, Mn is denoted in red, while O is denoted in green. The spectra contain the peaks corresponding to the Mn K_α and O K_α confirming the presence of manganese (Mn) and oxygen (O) indicating major contributions in the samples. The peak corresponding to carbon is due to the carbon tape used to place the sample to take measurements. The spectra display the uniform distribution of these elements pointing towards the formation of stoichiometric and homogeneous Mn_2O_3 nanoparticles.

Vibrational Spectroscopic Analysis

The identification of Mn species in manganese oxides corresponding to a particular phase is not easy by standard characterization tools only because manganese oxide exists in multiple phases including bixbyite, hausmannite, spinel, manganite, todorokite and many more.[47] The mixture of some of these phases might be present in the samples, few of which may result in the overlapping of Bragg's reflections.[47] Therefore, it becomes essential to support the outcomes of structural analysis with other competent techniques. Accordingly, Raman and FTIR spectroscopy has been employed to identify the phase and investigate the modification in the Mn-O and Mn-O-Mn vibrational modes of cubic Mn_2O_3 with respect to the PVP amount.

The Raman spectra of PVP assisted Mn_2O_3 nanoparticles are depicted in Fig. 5 in the spectral range of 200–1000 cm^{-1}. The vibrational modes in Raman spectra are due to the electron-phonon interactions caused by the incident radiation.[48] In general, the Raman spectra of Mn_2O_3 (bixbyite) result in five Raman active bands at 263, 308, 512, 631 and 670 cm^{-1} representing the out-of-plane vibrations in asymmetric and symmetric Mn-O-Mn species with bridging oxygen in which the high-intensity main band is observed at 631 cm^{-1}.[49,50] This band corresponds to the characteristic Raman frequency of vibrations in Mn-O Raman active modes of α-Mn_2O_3. In the present study, the samples exhibit the strong Raman active main bands in the range 631-635 cm^{-1} corresponding to α-Mn_2O_3. Moreover, the band frequencies resulting from the change in the local structure can be categorised in three different regions: corresponding to the wagging (200–450 cm^{-1}), bending (450–600 cm^{-1}) and stretching (600-750 cm^{-1}) of Mn-O Raman active modes. Therefore, the main band observed in the present case can be associated with the stretching vibrations of Mn-O.[35,51] The shifting in the Raman active bands with increasing PVP amount may be associated with the structural modifications relative to the PVP amount. Further, the intensity of the Raman bands is observed to be influenced significantly by the PVP amount. The intensity is found to first decrease for S2 as compared to S1 and then increase for S3 and S4 with increasing PVP amount. Thus, minimum intensity observed for S2 may be attributed to the reduced particle concentration and size of Mn_2O_3 nanoparticles.[52]

The FTIR spectra of Mn_2O_3 nanoparticles with different PVP amount is displayed in Fig. 6 within the range 400–4000 cm^{-1}. The spectra give information about the organic species present in the samples. The spectra display bands at 512, 570, 674, 1628 and 3437 cm^{-1} corresponding to stretching and bending vibrations. The bands observed at low wavenumbers, 512.4 and 674.2 cm^{-1} , correspond to the stretching vibrations of Mn-O and asymmetric stretching vibrations of Mn-O-Mn, respectively.[35] The band observed at 570 cm^{-1} is the characteristic band corresponding to the α-Mn_2O_3 phase.[51] The assignment of the peaks is in agreement with the published literature.[53] Karuppaiah et al. reported the two strong bands observed in the range 500–600 cm^{-1} correspond to the Mn-O vibrational modes.[20] Further, the FTIR bands at higher wavenumbers are due to the presence of hydroxyl groups.[54] Therefore, the bands observed at 1628.2 and 3437.4 cm^{-1} correspond to the bending and stretching modes of the O-H group.[41] The presence of the O-H group may be assigned to the water retained by the sample due to moisture absorption.[53] It is evident from the spectra that the peaks do not shift with respect to PVP amount indicating no change in the vibrational modes; however, the decrease in intensity of the 3437 cm^{-1} band has been observed and found to be lowest for S2, which indicates that

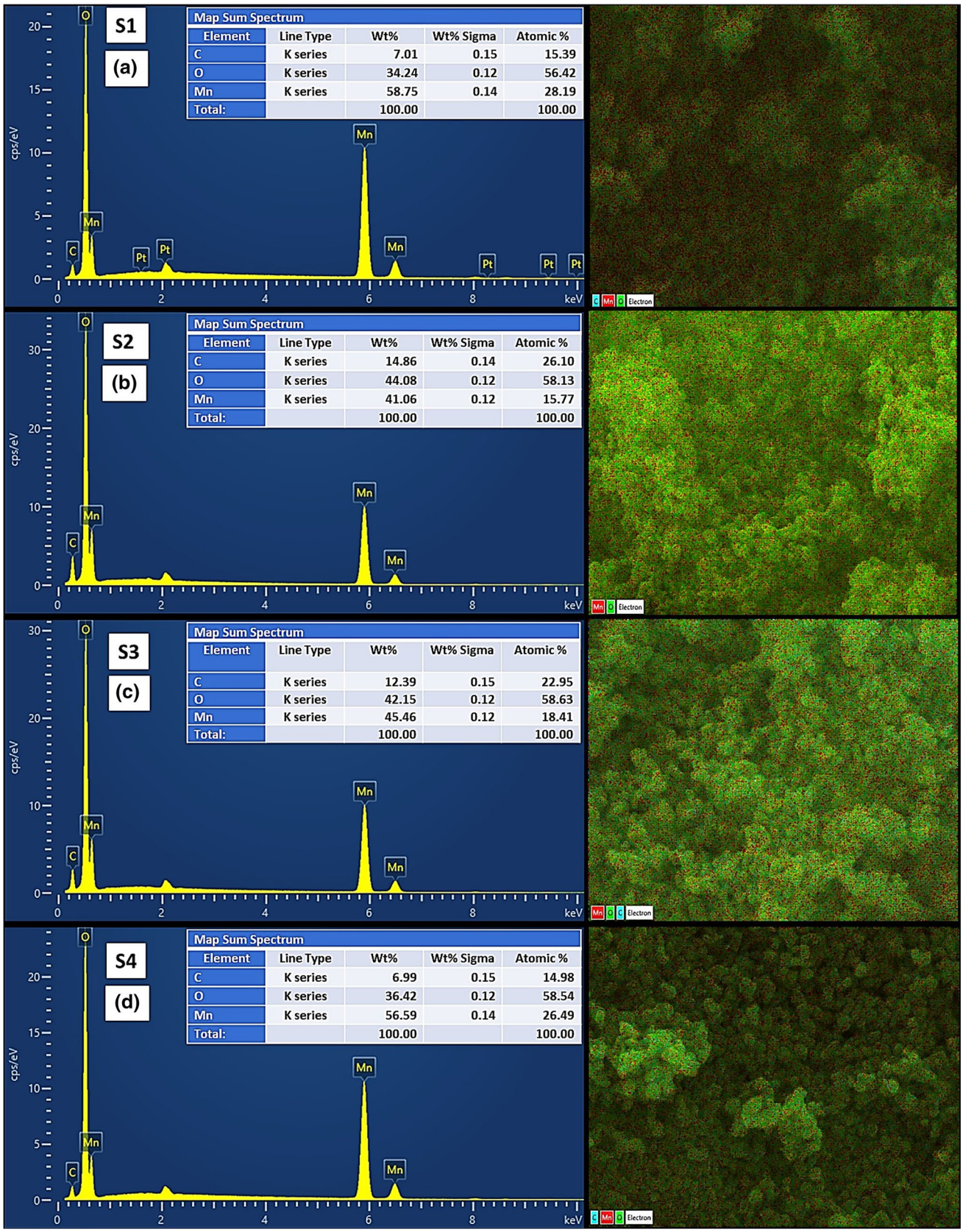

Fig. 4 (a–d) EDS spectra of samples S1 to S4 showing peaks corresponding to O K_α, Mn K_α and corresponding maps showing element distribution. Table indicating wt.%, wt.% sigma and at.% of the samples is demonstrated with the respective spectra.

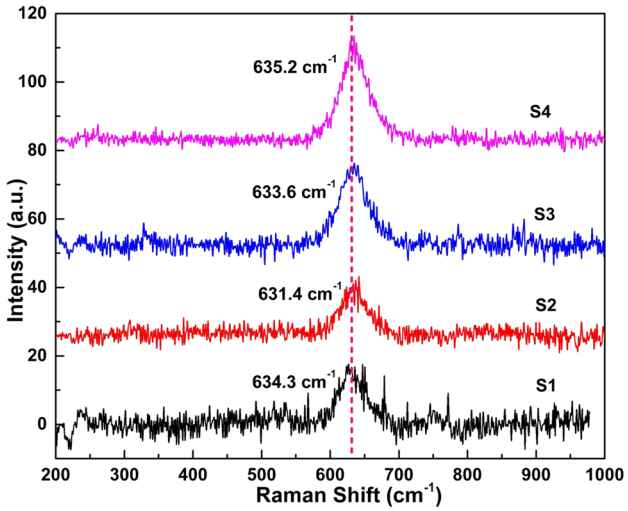

Fig. 5 Raman spectra showing characteristic Raman active band for Mn_2O_3 nanoparticles.

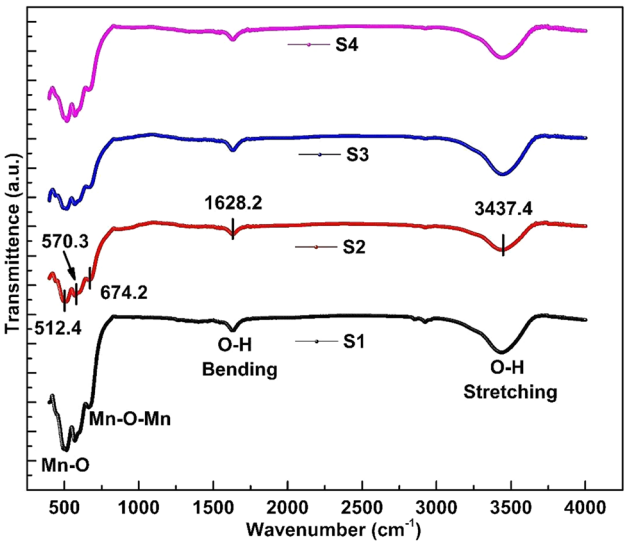

Fig. 6 FTIR spectra of samples from S1 to S4. Peaks ranging from 510 cm^{-1} to 680 cm^{-1} indicate the formation of Mn_2O_3 and peaks at higher wavenumber indicate the presence of a hydroxyl group.

a minimum quantity of O–H is present in S2. Further, no peak was detected corresponding to PVP indicating that the PVP has been evaporated during annealing. Thus, the FTIR analysis shows that all the samples exhibit similar spectra and confirm the single-phase formation of α-Mn_2O_3.

Magnetization

The antiferromagnetic nature of the α-Mn_2O_3 nanoparticles has been investigated through the temperature dependence of magnetic susceptibility (χ_m). The magnetic susceptibility of the samples was measured in the temperature range 50–380 K by applying an external magnetic field of 500 Oe under field-cooled (FC) and zero-field-cooled (ZFC) conditions as shown in Fig. 7a. The susceptibility is found to increase with decreasing temperature and becomes maximal at a temperature ~ 80 K indicating an inflection representing the blocking of spins resulting in decrease of susceptibility below 80 K. The temperature at which the susceptibility becomes maximum corresponds to the antiferromagnetic transition and is known as the Néel temperature (T_N).[3] The value of T_N ~80 K, observed in the present case, is as per the literature.[6] Interestingly, T_N observed for sample S1 is 81.8 K which decreases for S2 becoming 80.6 K and then again increases for S2 (81.3 K) and S3 (81.6 K). The value of T_N closer to the expected one (80 K) is observed for S2 (80.6 K). The variation trend of T_N is similar to the variation trend of the particle size indicating that the trivial change in T_N is attributable to the change in particle size. Thus, the increasing particle size also increases the antiferromagnetic transition temperature. In addition to the lowest T_N, the magnitude of the susceptibility is also found to be the lowest for S2. Also, sample S1 shows visible bifurcation which reduces for other samples. Further, the linear region of $1/\chi_m$ vs. temperature (T) is fitted using the Curie-Weiss law in order to find the paramagnetic Curie temperature (θ_P) as shown in Fig. 7b. The values of θ_P are indicated in Fig. 7b and found to follow the same trend as T_N. The values of θ_P and T_N have been used to find the magnetic frustration in the system by calculating the frustration parameter (f) using equation $f = \left|\frac{\theta_P}{T_N}\right|$ [3]. Figure 8a–b shows the field-dependent magnetization measurements of the samples in the range ±30 kOe performed at 300 K and 50 K. The samples exhibit paramagnetic behaviour at both temperatures where magnetization increases linearly with applied magnetic field. Further, the comparative analysis of θ_P, T_N and the frustration parameter (f) relative to the crystallite sizes is represented in Fig. 8c–f, which reveals that even though the variation in the magnetic parameters is small, it follows a similar trend in accordance with the crystallite sizes. This indicates that the PVP amount undeniably influences the magnetic properties of materials, albeit rather small.

Absorption Spectroscopy

The optical nature of the synthesized nanoparticles has been investigated using UV-vis absorption spectroscopy. The UV-Vis absorption spectra result from the transitions occurring in the material as a consequence of absorption of radiation. Figure 9a shows the UV-Vis spectra of samples S1-S4, recorded in absorption mode in the wavelength range 400–800 nm. The absorption edge for all the samples has been observed around 520 nm indicating the maximum

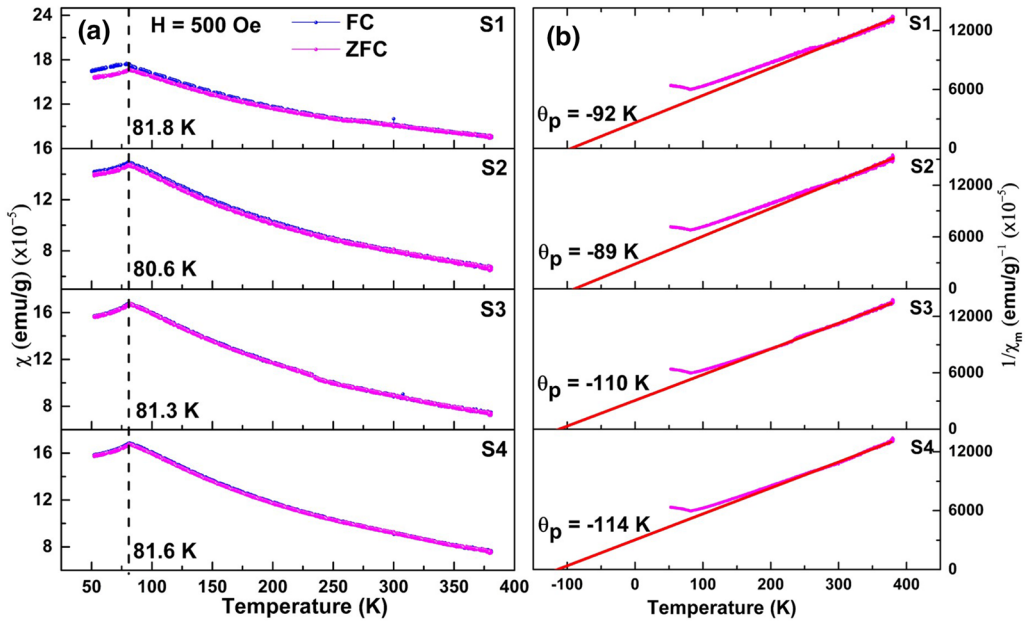

Fig. 7 (a) Temperature-dependent magnetic susceptibility (χ_m) obtained from field-cooled (FC) and zero-field-cooled (ZFC) temperature-dependent magnetization and (b) Variation of inverse of magnetic susceptibility with temperature fitted using the Curie-Weiss law to find the paramagnetic Curie temperature (θ_P).

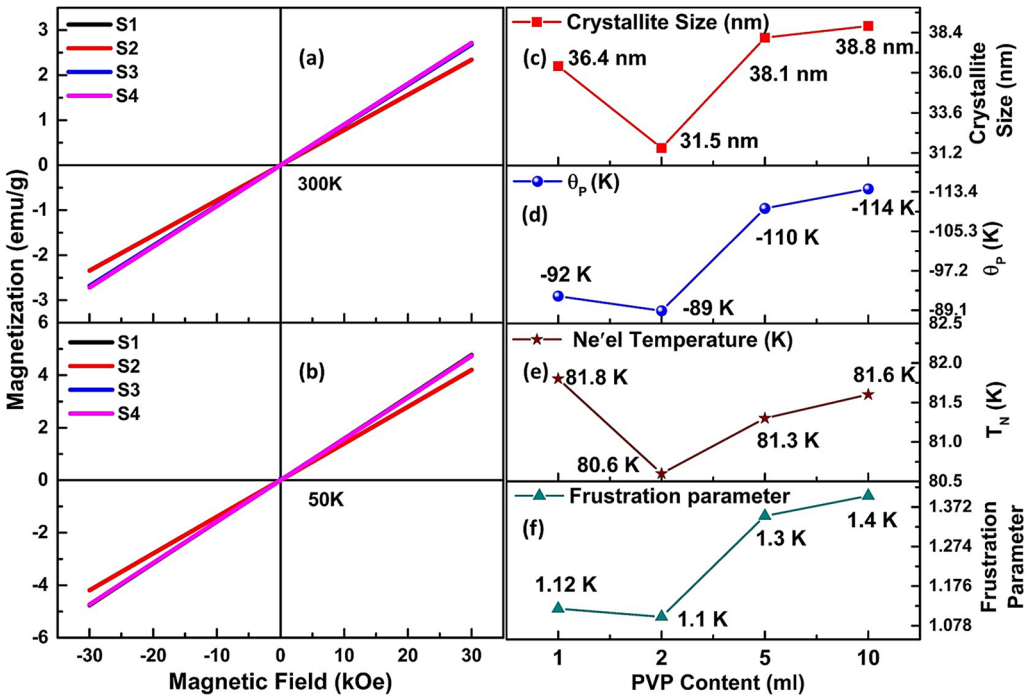

Fig. 8 Magnetic field-dependent magnetization at (a) 300 K, (b) 50 K, (c–f) comparative variation trend of crystallite sizes, paramagnetic Curie temperature (θ_P), Néel temperature (T_N) and frustration parameters.

absorption occurring in the visible range. After the maxima, the absorption reduces with increasing wavelength up to 650 nm above which it shows a slight increase. The energy corresponding to the absorption edge gives information about the energy required for the electronic transitions from the valence band to the conduction band.[55] The electronic

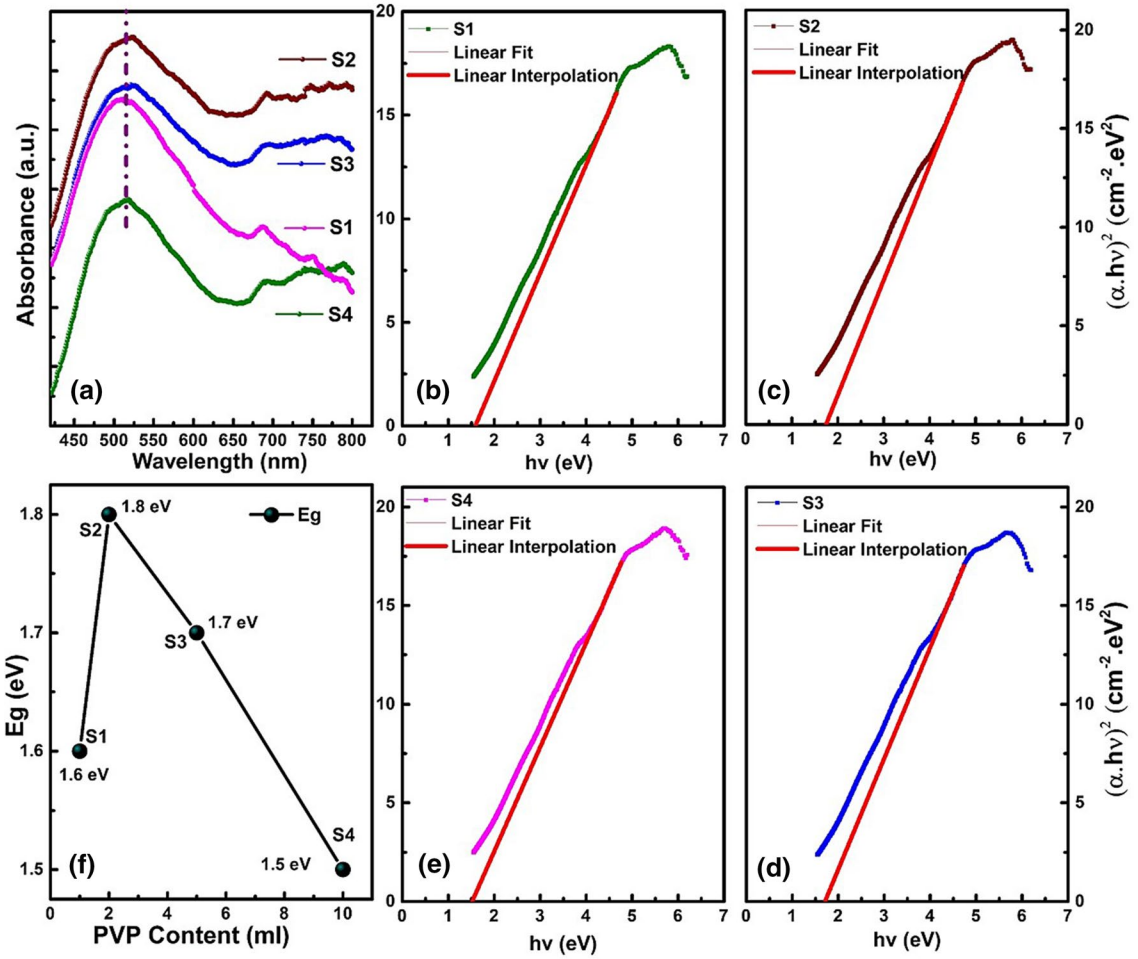

Fig. 9 (a) UV-Vis absorption spectrum of samples S1 to S4 as a function of wavelength showing maximum absorption for S2, (b–e) Fitting of absorbance using Tauc's equation to find the band gap, (f) Values of band gaps (E_g) obtained from the fitting of Tauc's equation.

transitions may be due to the charge transfer excitations or the crystal field transitions between the d-orbitals. The nature of the absorption curve further gives information about the type of transitions, direct or indirect. If the curve attains linearity after a certain value, then the band gap is considered the direct transition.[56] On the other hand, the presence of more than one bump indicates the occurrence of intermediate transitions revealing the indirect nature of the band gaps. Therefore, in the present case, the samples exhibit a direct band gap. The values of the direct band gap energies (E_g) in eV have been estimated by using the well-known Tauc's equation: $(\alpha h\nu)^2 = B(h\nu - E_g)$; where α is the absorption coefficient, hν is the photon energy and B is a constant.[57] Tauc's plots for the present samples are displayed in Fig. 9b–e. The point of intersection of the linear interpolation of the fitted linear region of the curve on the x-axis at zero absorption gives the value of the band gap energies which are indicated in Fig. 9f. All the samples exhibit band gaps in the range 1.5–2.0 eV. It is noticeable that Tauc's plot below the linear region is not smooth, rather it is slightly uneven or irregular. This may be attributed to the small but uneven increase in absorption above 650 nm. The value of band gap first increases from S1 to S2 and then decreases with increasing PVP amount. Thus, the band gap variation follows the similar trend as the particle size. The variation of the band gap with changing particle size is in accordance with the model presented by Singh et al.[58] According to this model, when the particle size decreases, as from S1 to S2 in the present case, the number of atoms forming the particle decreases. Therefore, the electron density of the valence band and the conduction band decreases due to which the spacing between the electronic states and band gap increases. On the other hand, when the particle size increases, as for S3 and S4, the number of atoms increases within the particle. This increases the density of electronic states and decreases the band gap. The phenomenon of band gap variation relative to the particle size has been demonstrated in Fig. 10. A similar effect has been reported by Alibe

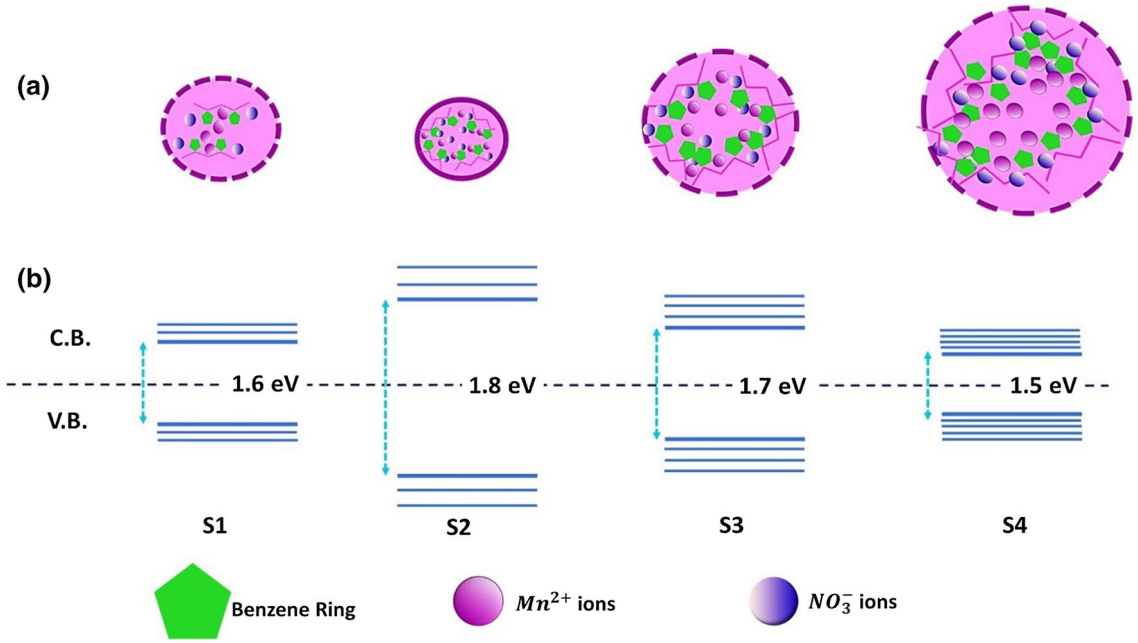

Fig. 10 Demonstration of band gap (E_g) variation relative to particle size variation.

et al. who observed the maximum band gap for the particles with minimum size.[45] Moreover, the values observed in the present case are smaller than the previously reported values. For instance, the band gap obtained by Gnanam et al. for cubic α-Mn_2O_3 nanoparticles was found to be in the range 3.36–3.49 eV,[5] whereas Amsaveni et al. determined a band gap of 2.1–2.2 eV for orthorhombic Mn_2O_3 nanoparticles.[4]

Mechanism of Nanoparticle Formation and the Limiting Behaviour of PVP

The possible mechanism for the nanoparticle formation is as follows: When manganese nitrate is dissolved in DI water, the Mn^{2+} ions are separated from NO^{3-} ions. After the ions dissolve, ammonia solution is added which provides hydroxide (OH^-) ions to Mn^{2+} to constitute the precipitates of manganese hydroxide ($Mn(OH)_2$). After that, when PVP solution is added, the amide group in PVP replaces the hydroxide anions and forms bonds with the metallic cations to eventually form the Mn_2O_3 nanoparticles. The attaching of the PVP chain limits the nanoparticles ability to expand in size and to agglomerate with other nanoparticles. The suppressing effect of PVP on the particle dimensions may be because the PVP chains increase the surface pressure and restrict the growth of particles. In the present case, this happens only up to 2 ml of PVP (S2). The suppressing boundaries also reduce the ionic concentration in the particle. The reduction in the ionic concentration of S2 can be verified through the Raman spectra in which the minimum intensity has been observed for S2 indicating minimum ionic concentration. However, as the PVP amount is increased beyond 2 ml, the number of ions attached to the PVP chain increases which increases the electron density and hence ionic concentration between the chains resulting in electrostatic repulsions among the neighbouring ions which further increases the particle size.[48] This phenomenon reveals the limiting behaviour of PVP chains which causes the structural and microstructural variations leading to the modification of the magnetic and optical properties. The schematic showing the formation of nanoparticles along with the involved chemical reactions and the variation in particle size is demonstrated in Fig. 11.

On one hand, the magnetic properties are very slightly altered as a function of PVP amount, while on the other hand, the optical properties exhibit a significant change. First of all, the values of band gaps observed for all the samples is smaller than the earlier reported values for Mn_2O_3 nanoparticles. Second, the maximum value of the band gap is observed for the particles with the smallest size (S2) which indicates an excellent assistance of PVP during synthesis.

Conclusions

In summary, PVP assisted α-Mn_2O_3 nanoparticles were prepared using co-precipitation method. The influence of PVP amount has been observed on the structural, microstructural, magnetic and optical properties. The synthesized nanoparticles were investigated using various characterization techniques viz. x-ray diffraction (XRD), high-resolution field emission scanning electron microscopy (HR-FESEM),

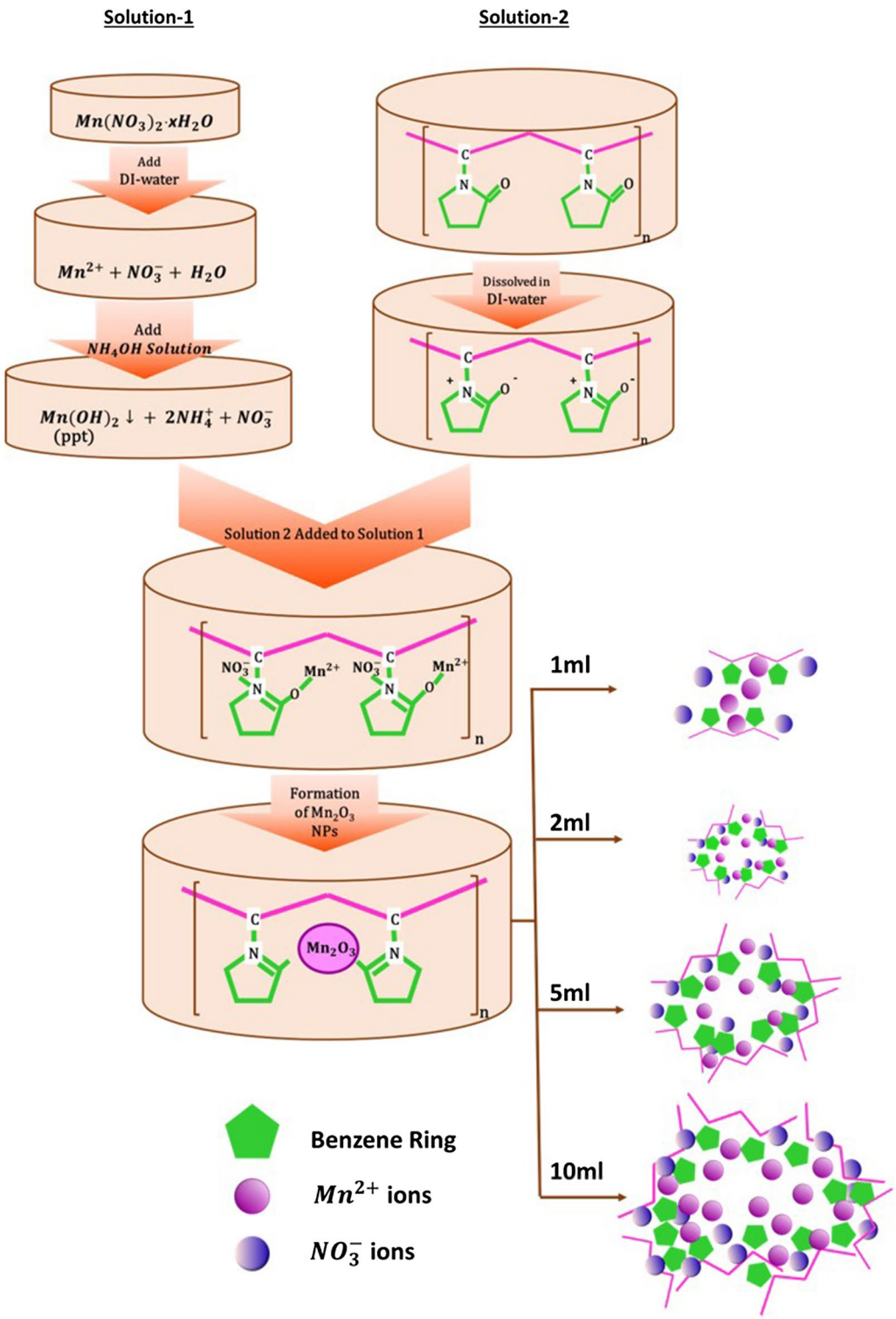

Fig. 11 Mechanism of nanoparticle formation along with the involved chemical equations.

energy dispersive x-ray spectroscopy (EDS), Raman spectroscopy, Fourier transform infrared (FTIR) spectroscopy, dc-magnetization and UV-vis absorption spectroscopy. From the interpretation of the results, the following conclusions can be drawn:

1. A PVP amount of 2 ml (S2) resulted in the smallest size α-Mn_2O_3 nanoparticles with smooth surface and spherical morphology. A PVP amount greater than 2ml increased the particle size and caused agglomeration in the particles.
2. Minimum magnetic frustration was observed for S2 corresponding to T_N = 80.6 K. Beyond 2 ml, the increase in PVP amount increased T_N as well as the magnetic frustration in the samples.
3. Assistance of PVP reduced the overall band gaps of the samples as compared to the observed literature, and maximum band gap (1.8 eV) was observed for the particles with lowest average size.

Acknowledgments Support for this project comes from the National Research Foundation of Korea grant funded by the Korean government (No. 2018R1D1A1B07046937).

Conflict of interest The authors have no conflict of interest.

References

1. X. Niu, H. Wei, K. Tang, W. Liu, G. Zhao, and Y. Yang, Solvothermal Synthesis of 1D Nanostructured Mn_2O_3: Effect of Ni^{2+} and Co^{2+} Substitution on the Catalytic Activity of Nanowires. *RSC Adv.* 5, 66271 (2015).
2. V. Subramanian, H. Zhu, and B. Wei, Nanostructured MnO_2: Hydrothermal Synthesis and Electrochemical Properties as a Supercapacitor Electrode Material. *J. Power Sources* 159, 361 (2006).
3. R.A.P. Ribeiro, M.C. Oliveira, E. Longo, S.R. de Lazaro, R. Nikam, P.S. Goyal, S. Radha, and S. Rayaprol, Magnetism and DFT Calculations for Understanding Magnetic Ground State of Fe Doped Mn_2O_3. *J. Alloys Compd.* 861, 158567 (2021).
4. P. Amsaveni, A. Nivetha, C. Sakthivel, C.S. Philip, and I. Prabha, Effectiveness of Surfactants for Unique Hierarchical Mn_2O_3 Nanomaterials as Enhanced Oxidative Catalysts, Antibacterial Agents, and Photocatalysts. *J. Phys. Chem. Solids* 144, 109429 (2020).
5. S. Gnanam and V. Rajendran, Facile Hydrothermal Synthesis of Alpha Manganese Sesquioxide (α-Mn_2O_3) Nanodumb-Bells: Structural, Magnetic, Optical and Photocatalytic Properties. *J. Alloys Compd.* 550, 463 (2013).
6. S.K. Ghosh, Diversity in the Family of Manganese Oxides at the Nanoscale : From Fundamentals to Applications. *ACS Omega* 5, 25493–25504 (2020).
7. N.E. Rajeevan, P.P. Pradyumnan, R. Kumar, D.K. Shukla, S. Kumar, A.K. Singh, S. Patnaik, S.K. Arora, and I.V. Shvets, Magnetoelectric Properties of $Bi_xCo_{2-X}MnO_4$ ($0 \le x \le 0.3$). *Appl. Phys. Lett.* 92, 111 (2008).
8. S.K. Sharma, R. Kumar, S. Kumar, V.V. Siva Kumar, M. Knobel, V.R. Reddy, A. Banerjee, and M. Singh, Magnetic Study of $Mg_{0.95}Mn_{0.05}Fe_2O_4$ Ferrite Nanoparticles. *Solid State Commun.* 141, 203 (2007).
9. G. Anjum, R. Kumar, S. Mollah, D. K. Shukla, S. Kumar, and C. G. Lee, Structural, Dielectric, and Magnetic Properties of $La_{0.8}Bi_{0.2}Fe_{1-X}Mn_xO_3$ ($0.0 \le x \le 0.4$) Multiferroics, *J. Appl. Phys.* 107, 0 (2010).
10. M.S. Anwar, S. Kumar, F. Ahmed, N. Arshi, G.W. Kim, and B.H. Koo, Above Room Temperature Magnetic Transition and Magnetocaloric Effect in $La_{0.66}Sr_{0.34}MnO_3$. *J. Korean Phys. Soc.* 60, 1587 (2012).
11. S.A. Ansari, N. Parveen, H.M. Kotb, and A. Alshoaibi, Hydrothermally Derived Three-Dimensional Porous Hollow Double-Walled Mn_2O_3 Nanocub Es as Superior Electrode Materials for Supercapacitor Applications. *Electrochim. Acta* 355, 136783 (2020).
12. L. Suryanti, S.E.I. Suryani, H. Hartatiek, N. Nasikhudin, J. Utomo, A. Taufiq, R. Suryana, Z. Aspanut, and M. Diantoro, The Effect of Mn_2O_3 Nanoparticles on Its Specific Capacitance of Symmetric Supercapacitors FC-ZnO-x (Mn_2O_3). *Mater. Today Proc.* 44, 3355 (2021).
13. M.S. Anwar, S. Kumar, F. Ahmed, N. Arshi, G.W. Kim, C.G. Lee, and B.H. Koo, Large Magnetic Entropy Change in $La_{0.55}Ce_{0.2}Ca_{0.25}MnO_3$ Perovskite. *J. Magn.* 16, 457 (2011).
14. M.S. Anwar, S. Kumar, F. Ahmed, S.N. Heo, G.W. Kim, and B.H. Koo, Study of Magnetic Entropy Change in $La_{0.65}Sr_{0.35}Cu_{0.1}Mn_{0.9}O_3$ Complex Perovskite. *J. Electroceramics* 30, 46 (2013).
15. J.H. Mokkath, M. Jahan, M. Tanaka, S. Tominaka, and J. Henzie, Temperature-Dependent Electronic Structure of Bixbyite α-Mn_2O_3 and the Importance of a Subtle Structural Change on Oxygen Electrocatalysis. *Sci. Technol. Adv. Mater.* 22, 141 (2021).
16. A. Indra, P.W. Menezes, F. Schuster, and M. Driess, Significant Role of Mn (III) Sites in e 1 g Configuration in Manganese Oxide Catalysts for Efficient Artificial Water Oxidation. *J. Photochem. Photobiol. B Biol.* 152, 156 (2015).
17. S. Geller, Structures of Alpha-Mn_2O_3, $(Mn_{0.983}Fe_{0.017})_2O_3$ and $(Mn_{0.37}Fe_{0.63})_2O_3$ and Relation to Magnetic Ordering. *Acta Cryst. B* 27, 821 (1971).
18. M. Sharrouf, R. Awad, M. Roumié, and S. Marhaba, Structural, Optical and Room Temperature Magnetic Study of Mn_2O_3 Nanoparticles. *Mater. Sci. Appl.* 6, 850 (2015).
19. M. Regulski, R. Przeniosło, I. Sosnowska, D. Hohlwein, and R. Schneider, Neutron Diffraction Study of the Magnetic Structure of α-Mn_2O_3. *J. Alloys Compd.* 362, 236 (2004).
20. M. Karuppaiah, P. Sakthivel, S. Asaithambi, R. Murugan, G. Anandha, R. Yuvakkumar, and G. Ravi, Solvent Dependent Morphological Modification of Micro-Nano Assembled Mn_2O_3/NiO Composites for High Performance Supercapacitor Applications. *Ceram. Int.* 45, 4298 (2019).
21. H. Ju, X.D. Liu, C.Y. Tao, F. Yang, X.L. Liu, X. Luo, and L. Zhang, Prussian Blue Analogue Derived Low-Crystalline Mn_2O_3/Co_3O_4 as High- Performance Supercapacitor Electrode. *J. Alloys Compd.* 856, 157134 (2021).
22. B.L. Vijayan, S.G. Krishnan, N.K.M. Zain, M. Harilal, A. Yar, I.I. Misnon, J.O. Dennis, M.M. Yusoff, and R. Jose, Large Scale Synthesis of Binary Composite Nanowires in the Mn_2O_3-SnO_2 System with Improved Charge Storage Capabilities. *Chem. Eng. J.* 327, 962 (2017).
23. Z.H. Wang, D.Y. Geng, W.J. Hu, W.J. Ren, and Z.D. Zhang, Magnetic Properties and Exchange Bias in Mn_2O_3/Mn_3O_4 Nanoclusters. *J. Appl. Phys.* 105, 07A315 (2009).
24. E. Cockayne, I. Levin, H. Wu, and A. Llobet, The Magnetic Structure of Bixbyite α-Mn_2O_3: A Combined Density Functional Theory DFT+U and Neutron Diffraction Study. *Phys. Rev. B* 87, 184413 (2013).
25. S. Jana, Advances in Nanoscale Alloys and Intermetallics: Low Temperature Solution Chemistry Synthesis and Application in Catalysis. *Dalt. Trans.* 44, 18692 (2015).
26. M.F. Silva, L.A.S. De Oliveira, M.A. Ciciliati, M.K. Lima, F.F. Ivashita, D.M. Fernandes De Oliveira, A.A.W. Hechenleitner, and E.A.G. Pineda, The Effects and Role of Polyvinylpyrrolidone on the Size and Phase Composition of Iron Oxide Nanoparticles Prepared by a Modified Sol-Gel Method. *J. Nanomater.* 2017, 17 (2017).

27. P. Díaz-Núñez, J. González-Izquierdo, G. González-Rubio, A. Guerrero-Martínez, A. Rivera, J.M. Perlado, L. Bañares, and O. Peña-Rodríguez, Effect of Organic Stabilizers on Silver Nanoparticles Fabricated by Femtosecond Pulsed Laser Ablation. *Appl. Sci.* 7, 793 (2017).
28. N. Arshi, F. Ahmed, S. Kumar, M.S. Anwar, B.H. Koo, and C.G. Lee, Comparative Study of the Ag/PVP Nanocomposites Synthesized in Water and in Ethylene Glycol. *Curr. Appl. Phys.* 11, S346 (2011).
29. J. Tientong, S. Garcia, C.R. Thurber, and T.D. Golden, Synthesis of Nickel and Nickel Hydroxide Nanopowders by Simplified Chemical Reduction. *J. Nanotechnol.* 2014, 1 (2014).
30. A. Khort, S. Roslyakov, and P. Loginov, Solution Combustion Synthesis of Single-Phase Bimetallic Nanomaterials. *Nano-Struct. Nano-Objects* 26, 100727 (2021).
31. J. Li, K. Inukai, Y. Takahashi, A. Tsuruta, and W. Shin, Effect of PVP on the Synthesis of High-Dispersion Core-Shell Barium-Titanate–Polyvinylpyrrolidone Nanoparticles. *J. Asian Ceram. Soc.* 5, 216 (2017).
32. J. Rodríguez-carvajal, Recent Developments of the Program FULLPROF, in Commission on Powder Diffraction, (IUCr). *Newsl.* 26, 12 (2001).
33. G. Will, *Powder Diffraction the Rietveld Method and the Two Stage Method to Determine and Refine Crystal Structures from Powder Diffraction Data* (Berlin Heidelberg: Springer-Verlag, 2006).
34. Y. Li, L. Liu, L. Liu, Y. Liu, H. Zhang, and X. Han, Efficient Oxidation of Phenol by Persulfate Using Manganite as a Catalyst. *J. Mol. Catal. A Chem.* 411, 264 (2016).
35. Y. Son, P.T.M. Bui, H. Lee, M.S. Akhtar, D.K. Shah, and O. Yang, A Rapid Synthesis of Mesoporous Mn_2O_3 Nanoparticles for Supercapacitor Applications. *Coatings* 9, 631 (2019).
36. B.H. Toby, *Chapter 4.7. Rietveld Refinement*, in *International Tables for Crystallography Volume H: Powder Diffraction* (Wiley, 2019), pp. 465–472.
37. B.H. Toby, R Factors in Rietveld Analysis: How Good is Good Enough? *Powder Diffr.* 21, 67 (2006).
38. L.B. Mccusker, R.B. Von Dreele, D.E. Cox, D. Louer, and P. Scardi, Rietveld Refinement Guidelines. *J. Appl. Cryst.* 32, 36 (1999).
39. K. Kumari, R.N. Aljawfi, Y.S. Katharria, S. Dwivedi, K.H. Chae, R. Kumar, A. Alshoaibi, P.A. Alvi, S. Dalela, and S. Kumar, Study the Contribution of Surface Defects on the Structural, Electronic Structural, Magnetic, and Photocatalyst Properties of Fe: CeO_2 Nanoparticles. *J. Electron Spectros. Relat. Phenomena* 235, 29 (2019).
40. F. Jiao, A. Harrison, A.H. Hill, and P.G. Bruce, Mesoporous Mn_2O_3 and Mn_3O_4 with Crystalline Walls. *Adv. Mater.* 19, 4063 (2007).
41. R. Najjar, R. Awad, and A.M. Abdel-Gaber, Physical Properties of Mn_2O_3 Nanoparticles Synthesized by Co-Precipitation Method at Different PH Values. *J. Supercond. Nov. Magn.* 32, 885 (2019).
42. S. Kumar, K. Kumari, F.A. Alharthi, F. Ahmed, R. Naji, P.A. Alvi, R. Kumar, M. Hashim, and S. Dalela, Investigations of TM (Ni, Co) Doping on Structural, Optical and Magnetic Properties of CeO_2 Nanoparticles. *Vacuum* 181, 109717 (2020).
43. D. Nath and R. Das, Experimental (XRD) and Theoretical (DFT) Analysis for Understanding the Influence of SHI Irradiation on the Stacking Fault Energy in CdSe Nanocrystals. *J. Alloys Compd.* 879, 160456 (2021).
44. A.J. Deotale and R.V. Nandedkar, Correlation Between Particle Size, Strain and Band Gap of Iron Oxide Nanoparticles. *Mater. Today Proc.* 3, 2069 (2016).
45. I.M. Alibe, K.A. Matori, H.A.A. Sidek, Y. Yaakob, U. Rashid, A. Mustapha, M. Hafiz, M. Zaid, S. Nasir, and M. Mohammed, Effects of Polyvinylpyrrolidone on Structural and Optical Properties of Willemite Semiconductor Nanoparticles by Polymer Thermal Treatment Method. *J. Therm. Anal. Calorim.* 136, 2249 (2019).
46. S. Dagar, A. Hooda, S. Khasa, and M. Malik, Rietveld Refinement, Dielectric and Magnetic Properties of NBT-Spinel Ferrite Composites. *J. Alloys Compd.* 806, 737 (2019).
47. S. Bernardini, F. Bellatreccia, A.C. Municchia, G. Della Ventura, and A. Sodo, Raman Spectra of Natural Manganese Oxides. *J Raman Spectrosc.* 50, 1 (2019).
48. A.C. Ferrari, S.E. Rodil, and J. Robertson, Interpretation of Infrared and Raman Spectra of Amorphous Carbon Nitrides. *Phys. Rev. B* 67, 155306 (2003).
49. C.M. Julien, M. Massot, and C. Poinsignon, Lattice Vibrations of Manganese Oxides Part I. Periodic Structures. *Spectrochim. Acta Part A* 60, 689 (2004).
50. A.H.A.M. Videla, L. Osmieri, R.A.M. Esfahani, J. Zeng, C. Francia, and S. Specchia, The Use of C-MnO_2 as Hybrid Precursor Support for a Pt/C-Mn_xO_{1+x} Catalyst with Enhanced Activity for the Methanol Oxidation Reaction (MOR). *Catalysts* 5, 1399 (2015).
51. F. Buciuman, F. Patcas, R. Craciun, and D.R.T. Zahn, Vibrational Spectroscopy of Bulk and Supported Manganese Oxides. *Phys. Chem. Chem. Phys.* 1, 185 (1999).
52. L. Slavov, M.V. Abrashev, T. Merodiiska, C. Gelev, R.E. Vandenberghe, I. Markova-Deneva, and I. Nedkov, Raman Spectroscopy Investigation of Magnetite Nanoparticles in Ferrofluids. *J. Magn. Magn. Mater.* 322, 1904 (2010).
53. L. Jayaselvan and C. Gnanasambandam, Structural, Optical and Phase Formation Modifications by Varying Precursor Temperature on Mn_2O_3 Nanoparticles Prepared by Microwave Assisted Precipitation. *AIP Conf. Proc.* 2311, 080008 (2020).
54. A. Filtschew, K. Hofmann, and C. Hess, Ceria and Its Defect Structure : New Insights from a Combined Spectroscopic Approach. *J. Phys. Chem. C* 120, 6694–6703 (2016).
55. A. Vijayamari, K. Sadayandi, S. Sagadevan, and P. Singh, A Study of Optical, Surface Morphological and Electrical Properties of Manganese Oxide Nanoparticles. *J. Mater. Sci. Mater. Electron.* 28, 2739 (2017).
56. S. Li, Y.H. Lin, B.P. Zhang, Y. Wang, and C.W. Nan, Controlled Fabrication of $BiFeO_3$ Uniform Microcrystals and Their Magnetic and Photocatalytic Behaviors. *J. Phys. Chem. C* 114, 2903 (2010).
57. S. Kumar, M. Sharma, R.R.N., K.H. Chae, R. Kumar, S. Dalela, A. Alshoaibi, F. Ahmed, and P.A. Alvi, Tailoring the Structural, Electronic Structure and Optical Properties of Fe: SnO_2 Nanoparticles, *J. Electron Spectros. Relat. Phenomena* **240**, 146934 (2020).
58. M. Singh, M. Goyal, and K. Devlal, Size and Shape Effects on the Band Gap of Semiconductor Compound Nanomaterials. *J. Taibah Univ. Sci.* 12, 1 (2018).